# A structural and optical modification of ZnO-$Fe_2O_3$ nanocomposite for enhancing catalytic activity

A. Rehman [a], M. Boota [a,*], M. I. Khan [a], A. Hussain [a], S. Kanwal [a], M. Atif [b], I. Ahmad [c]
[a] *Department of Physics, The University of Lahore, 53700, Pakistan*
[b] *Department of Physics and Astronomy, College of Science, King Saud University, P O Box 2455, Riyadh 11451, Saudi Arabia*
[c] *Department of Physics and Astronomy, Texas Tech University, Lubbock, TX 79409, USA*

This study investigates the photocatalytic degradation of organic Methyl Blue (MB) using a ZnO-$Fe_2O_3$ composite prepared via the sol-gel technique. FTIR analysis elucidates the substantial impact of $Fe_2O_3$ addition, as evidenced by shifts in the ZnO absorption bands, notably observed at 631 $cm^{-1}$ and 919.74 $cm^{-1}$ peaks. X-ray diffraction (XRD) corroborates heightened crystallinity due to interactions between ZnO and $Fe_2O_3$. SEM analysis unveils a highly aggregated structure, showcasing promising capabilities for efficient dye degradation and environmental applications. Photoluminescence (PL) spectra exhibit an intensified peak at 377 nm, indicative of efficient charge separation and electron transfer, offering potential in optoelectronic applications. The composite's distinctive refractive index (n) of 2.33, extinction coefficient (k) of 2.12, optical electronegativity (ΔX*) of 0.75, and dielectric constants (εr of 0.40 and εi of 9.92) underscore its versatile bonding and broad application prospects. Evaluating the photocatalytic activity (PCA) reveals that among all samples, the nanocomposite ZnO-$Fe_2O_3$ synthesized at 500°C exhibits superior performance, showcasing heightened degradation of MB dye under 90 minutes of sunlight irradiation.

(Received June 3, 2024; Accepted October 7, 2024)

*Keywords:* Methyl blue, ZnO, $Fe_2O_3$, Nanocomposite, Degradation of dye

## 1. Introduction

The explosive growth of the economy has exacerbated many problems related to water contamination worse, particularly those involving organic pollutants. People have devoted their life to managing the environment through the use of renewable energy sources [1]. Many renewable energy sources, like the sun, wind, and hydropower, use the Earth's natural processes to generate electricity in an environmentally friendly way. These renewable energy sources contribute to our overall reduction of non-renewable resource usage by providing plentiful, clean, and ecologically friendly substitutes for finite fossil fuels like coal [2]. A sustainable and environmentally beneficial future depends on the adoption of these clean energy sources. The sun is the most consistent and dependable of all these renewable energy sources. Solar power, which comes from the sun's infinite energy, is said to be the best renewable energy source since it is always available. Moreover, a variety of chemical (ion exchange, advanced oxidation processes and reverse osmosis), biologically (respiratory and anaerobically deterioration), and physically (ozone formation, precipitation, adsorption, and filters with coagulation) strategies have been used to address the issue of organic pollutants [3]. Photocatalysis has generated significant interest in both energy and the removal of environmental pollutants. According to a summary of photocatalysis, when solar energy is more than or equal to the semiconductor's bandgap, while electron in the band gap (VB) emit energy and moved into the band known as conduction band. The hydroxyl radical, which is a component of the H2O system, is produced by the hole's sufficient oxygen supply, which allows it to oxidize different

* Corresponding author: muhammad.boota@phys.uol.edu.pk
https://doi.org/10.15251/JOR.2024.205.703

organic pollutants. When the superoxide radical, which forms when the CB's electrons react with $O_2$ in $H_2O$, makes a bond with the OH ion, the radical of hydroxyl (•OH) in water is formed. The hole has the ability to oxidize various organic contaminants and generate a •OH radical in water. The organic molecules in the contaminants are oxidized by this potent oxidant, •OH, rendering them inert [4] Figure 1. In wastelands, a variety of novel photocatalysts, such as tungsten trioxide [5], zirconia[6], vanadium oxide [7], iron oxide[6], titanium dioxide[8], and zinc oxide[9], have been used in a dynamic manner. The main reasons are its excellent photocatalytic activity, broad UV bandgap energy of about 3.2 eV, affordability, higher free-exciton binding energy, and oxidation capacity. Despite its enhanced photocatalytic efficiencies, its poor quantum yield due to the faster coupling of photo generated electron and hole pairs still makes it difficult for it to meet the requirements for real-world applications. Furthermore, ZnO is less suitable for Photocatalysis of visible light since its band gap lies in the UV region.

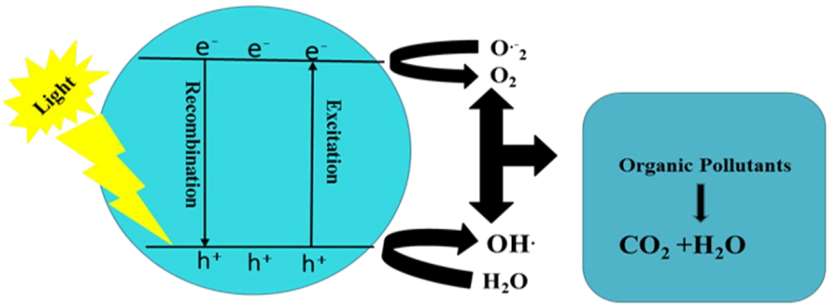


*Fig. 1. Mechanism of photocatalysis.*

However, low diffusion and agglomeration limit the primary applications of all metal oxides, and different approaches must often be taken before the composite is created in order to boost the efficiency of the nanoparticles. With their extensive experience in metal oxide doping, especially with ions such as FeO, CoO, and NiO, our research group is able to synthesize doped ZnO nanomaterials with a range of structural and morphological features [10]. Among all FeO is much more suitable to degrade MB because of its smaller band gap of about 2.2 eV. $Fe_2O_3$ can thus absorb a significant amount of the visible solar spectrum (absorbance edge ~600 nm). Its benign nature, low cost, abundance, and strong chemical stability in aqueous medium make it an attractive material for applications such as water splitting and photocatalytic water treatment[11]. When additional nanomaterials are present, ZnO nanocomposites affect charge transfer reactions at the interface and improve charge separation, giving rise to unique features of the nanocomposite[12]. The control of piezoelectricity may benefit from these variances. Nam et al.'s study examined the phase transitions and physical characteristics of non-native transition metal oxides, such as cubic FeO, NiO, and hexagonal ZnO[13]. The hexagonal crystal structure of ZnO, which has tetrahedrally linked $Zn^{2+}$ cations and $O^{2-}$ anions, supports the material's intrinsic piezoelectricity.

In our pursuit of elevating dye degradation efficiency, we embarked on a groundbreaking synthesis of $Fe_2O_3$/ZnO nanocomposites. Within this alchemy of materials, $Fe_2O_3$ emerges as a captivating protagonist boasting not only favorable electrical properties but also a tantalizingly slower recombination rate compared to ZnO [14]. This enigmatic allure hints at a potential enhancement within the intricate dance of the photocatalytic mechanism. While ZnO confidently captures UV light with its formidable band gap energy, $Fe_2O_3$ gracefully ensnares the elusive visible light. The resulting composite paints a canvas that absorbs a sweeping swath of both UV and visible light spectra—a mesmerizing fusion in the realm of photocatalysis. Yet, as any virtuoso knows, flaws can dim even the brightest performances. ZnO, while impressive in its photoctalytic activity, falters under the weight of a high recombination rate, threatening its efficiency. Enter $Fe_2O_3$, with its graceful poise and low recombination rate, poised to join forces and choreograph a symphony that mitigates the recombination, allowing ZnO to shine brighter than ever before. But the climax of this composition doesn't end there. The magnetic allure of $Fe_2O_3$ adds an unexpected twist—

transforming this composite into a magnetic maestro. A simple sweep of an external magnetic field elegantly retrieves and readies the composite for an encore, minimizing both cost and time while orchestrating an environmentally conscious performance. This composite, a veritable symphony of scientific ingenuity, promises not just enhanced efficiency but an ode to sustainability and resourcefulness in its every encore.

## 2. Experimental setup

### 2.1. Synthesis of ZnO/$Fe_2O_3$ nanocomposites

The green extract of ginger was obtained by the same previous published paper[15]. The synthesis of ZnO required the addition of two precursors into 150 ml of ginger solution; one is zinc acetate dehydrate (Sigma Aldrich), 0.025 mol (5.48g), and second is hexamethylene tetra amine, 0.025mol (3.6g), using the sol-gel method. The $Fe_2O_3$ was prepared by using (2.7g) of ferric chloride hexahydrate. The mixture was agitated at 90°C for six hours. After then, ethanol and deionized water were used to clear the precipitates several times. The samples were dried at 100 $^oC$ for 24 hours.

A 1:1wt% ratio of $Fe_2O_3$ to ZnO ($FeCl_3$.6 $H_2O$), 0.01mol (2.7g) of ferric chloride hexahydrate, and 0.01mol (0.87g) of zinc oxide powder were combined to create a ZnO-$Fe_2O_3$ mixed nanocomposite in 100ml of ginger solution. The pH of the solution was 2.0 until ammonia ($NH_3$), acting as a precipitating agent and added drop by drop to the base solution while being continuously agitated, brought the pH of the solution up to 10. The resulting precipitates were filtered, and then repeatedly washed with ethanol and deionized water. It was then dried in a vacuum oven at 80°C for thirty hours. ZnO-$Fe_2O_3$ nanoparticles were finally calcined for five hours at 500 °C in the air.

### 2.2. Characterization

To examine the structural properties of NPs, an X-ray diffractometer (Rigaku Diffractometer) is utilized, which has an X-ray wavelength of =0.154 nm. For usage in FTIR research, the Nicolet Nexus 870 FT-IR spectrometer was equipped with a deuterated triglycine sulphate detector, courtesy of Nicolet Instrument Corp. of Madison, Wisconsin, USA. High-resolution spectral data across a range of wavelengths are concurrently captured using an FTIR spectrophotometer. The material's composition was ascertained using a scanning electron microscope (SEM, Nova-400). The optical characteristics were assessed using a UV2102PC spectrophotometer.

## 3. Result and discussion

The crystalline characteristics of $Fe_2O_3$, ZnO, and ZnO-$Fe_2O_3$ nanoparticles are investigated by XRD, as shown in Figure 2. It can be seen from XRD pattern of sample ZnO that a sharp peaks was observed at 2θ=31.74°, 34.39°, 36.24°, 47.52°, 56.52°, 62.87°, 66.36°,67.95°,69.06° and 76.82°, all of which correspond to a hexagonal structure (PDF: 79-0206). Corresponding to (hkl) planes (100), (002), (101), (102), (110), (103), (200), (112), (201) and (202). According to PDF: 79–2381), the Rhombohedral structure of $Fe_2O_3$ is shown by the distinctive diffraction peaks at 2θ =24.34°, 33.43°, 35.94°, 41.0°, 54.35°, 57.99°, 62.71°, and 72.16° corresponds to hkl planes (012), (104), (110), (113), (116), (018), (214), and (101). The above-mentioned peaks are visible in the XRD patterns of the nanocomposite, but no secondary impurity phases are visible. Peaks of $Fe_2O_3$ and ZnO are seen in nanocomposite. The enhanced ZnO-$Fe_2O_3$ peak intensity verifies that ZnO and $Fe_2O_3$ interacts with one another and enhances the crystallinity of the nanocomposite. The nanocomposite's high peak intensity may have resulted from the aromatic system's preference for ZnO at the crystal nucleation center, which led to the formation of a nanocomposite with larger particles.

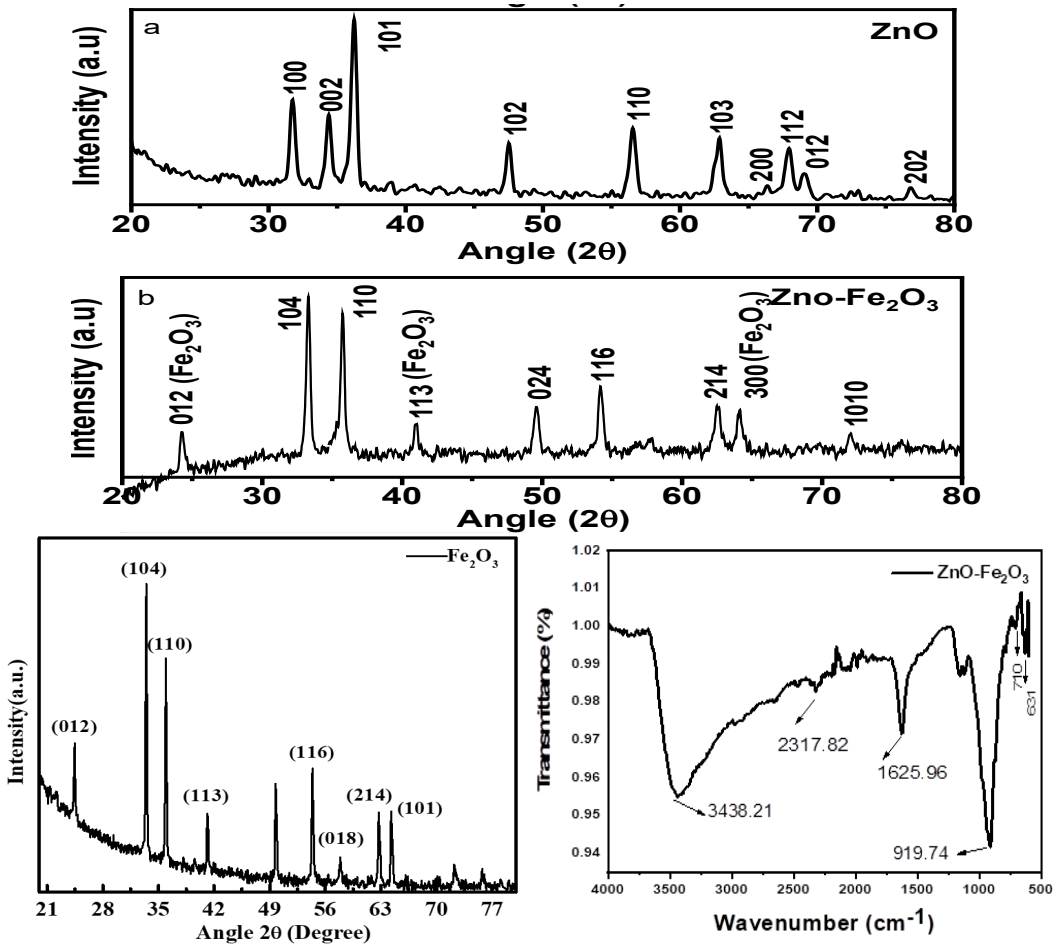


*Fig. 2. XRD of ZnO, $Fe_2O_3$, and ZnO-$Fe_2O_3$, FTIR spectra of ZnO-$Fe_2O_3$ nano composite prepared by sol-gel method annealed at 500°C.*

Grain size (D) is calculated by scherrer formula[2];

$$D = 0.9\lambda/B\cos\Theta \quad (1)$$

Grain size of ZnO is 28 nm, $Fe_2O_3$ is 24 nm and ZnO-$Fe_2O_3$ is 34 nm. ZnO and $Fe_2O_3$ have varied grain sizes throughout the nanocomosite production process; new grains are formed when two planes get close to one another. The diameters of the new grains range greatly since their nucleation occurs at different times and their growth rates are distinct. The enhanced grain size in the ZnO-$Fe_2O_3$ nanocomposite, as compared to pure ZnO nanoparticles, can be attributed to the presence of α-$Fe_2O_3$ acting as a stabilizing agent[16]. Pure ZnO nanoparticles tend to experience uncontrolled grain growth over time, resulting in larger grains with a less regulated crystalline structure[17]. However, the inclusion of α-$Fe_2O_3$ inhibits this uncontrolled grain growth by serving as a nucleation site and grain growth barrier. The controlled grain size in the nanocomposite holds particular significance for photocatalysis applications, optimizing the material's efficiency in utilizing light energy for catalytic reactions, making it well-suited for various environmental and energy-related applications where efficient light absorption and reaction kinetics are essential. Figure 2d displays the synthesized nanostructures' FTIR spectra. The first peak at 631 $cm^{-1}$ represents the $Fe_2O_3$ vibrational modes, which are located between 600 and 700 $cm^{-1}$. The peak at 919.74 $cm^{-1}$ served as a signal for the dispersion of $Fe_2O_3$ molecules into the ZnO lattice. In the absorption band at 1625.96 $cm^{-1}$, the C=O bond was discernible[18]. As a result, an extensive O-H peak was found at 3438.21 $cm^{-1}$. Interestingly, it was found that the increase in $Fe_2O_3$ doping

concentration caused a shift in the ZnO absorption band, which had a substantial effect on the FTIR spectra. The fact that the doping process was directly responsible for this shift in the location of the absorption band emphasizes how important the doping concentration is for altering peak intensities within spectra.

The morphological feature of synthesized $ZnO/Fe_2O_3$ nano-composites is presented in Figure 3.

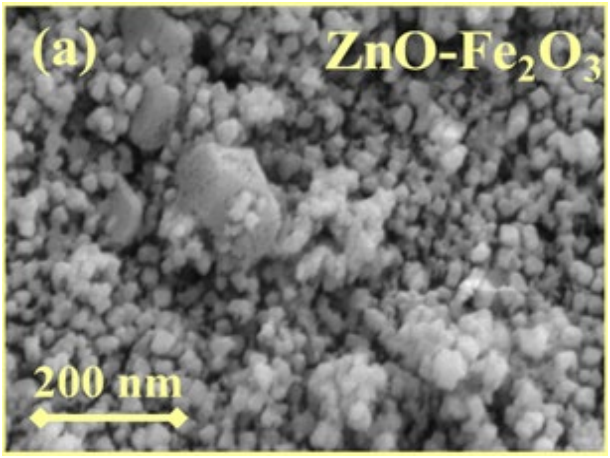


*Fig. 3. SEM of $ZnO$-$Fe_2O_3$ nano-composite.*

The morphology of ZnO is seen in Figure 3, where an agglomerated structure is produced by tightly packed nanoparticles.

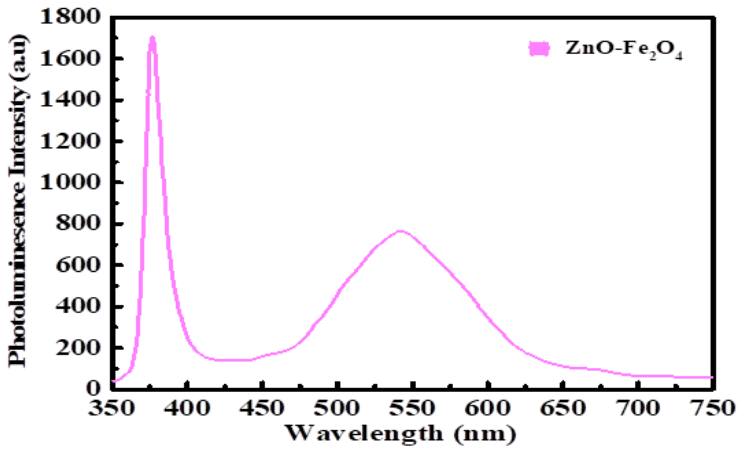


*Fig. 4. Photo luminance of $ZnO$-$Fe_2O_3$ nanocomposites.*

Individual nanoparticles stack as a result of this aggregation, which is driven by weak attractive forces like van der Waals interactions and eventually forms larger clusters or agglomerates. ZnO powder is characterized by the compact arrangement of individual nanoparticles within these clusters. The produced $ZnO/Fe_2O_3$ nano-composite exhibits an impressive and homogeneous morphology with well-defined size and a significant level of aggregation, clearly demonstrating the coexistence of ZnO and $Fe_2O_3$ components [19, 20]. This particular surface structure which is typified by a large-scale aggregation of nanoparticles is essential for improving the material's dye degradation efficiency. Increased dye adsorption and thus better catalytic performance are made possible by the complex network of aggregated nanomaterials, which increases surface area. Significantly, because of the larger surface area, which provides more sites

for efficient light absorption and subsequent catalytic reactions, this surface creation promotes the photolytic phenomena. This physical characteristic, the marked aggregation, is a distinctive trait that highlights the remarkable efficacy of the nano-composite in promoting dye degradation, thereby positioning it as a viable option for advanced applications in wastewater treatment and environmental remediation.

The charge separation and charge recombination processes of the photoinduced electron-hole pairs were also examined using the PL spectra [41]. It was discovered that the rate of recombination of the photo induced electron–hole pairs is proportional to the PL intensity. Figure 4 shows the PL spectra of ZnO-$Fe_2O_3$ nanocomposites performed at an excitation wavelength of around 360 nm. ZnO-$Fe_2O_3$ nanocomposites' PL behavior displays different optical phenomena that are inherent in their composition, structural attributes, and bonding interactions. The nanocomposite of ZnO and $Fe_2O_3$ enhances PL emission and promotes efficient electron transfer, facilitated by the presence of robust covalent and charge transfer bonds between these materials. This increased radiative recombination rate is indicated by the elevated intensity at 377 nm, as surface defect states act as effective radiative recombination centers, thereby amplifying the photoluminescence intensity [21]. The weaker peak at 540 nm is associated with $Fe_2O_3$ emissions, suggesting a lower radiative recombination rate due to unique iron-oxygen bonding [22]. These findings underscore the influence of composition, defect states, and bonding interactions in nanocomposites, offering prospects for optoelectronic applications and emphasizing their significance in nanomaterial research.

UV-Vis spectrophotometry is used to study the optical properties of the synthesized samples. The absorbance against the wavelength spectra for ZnO-$Fe_2O_3$ is shown in Figure 5.

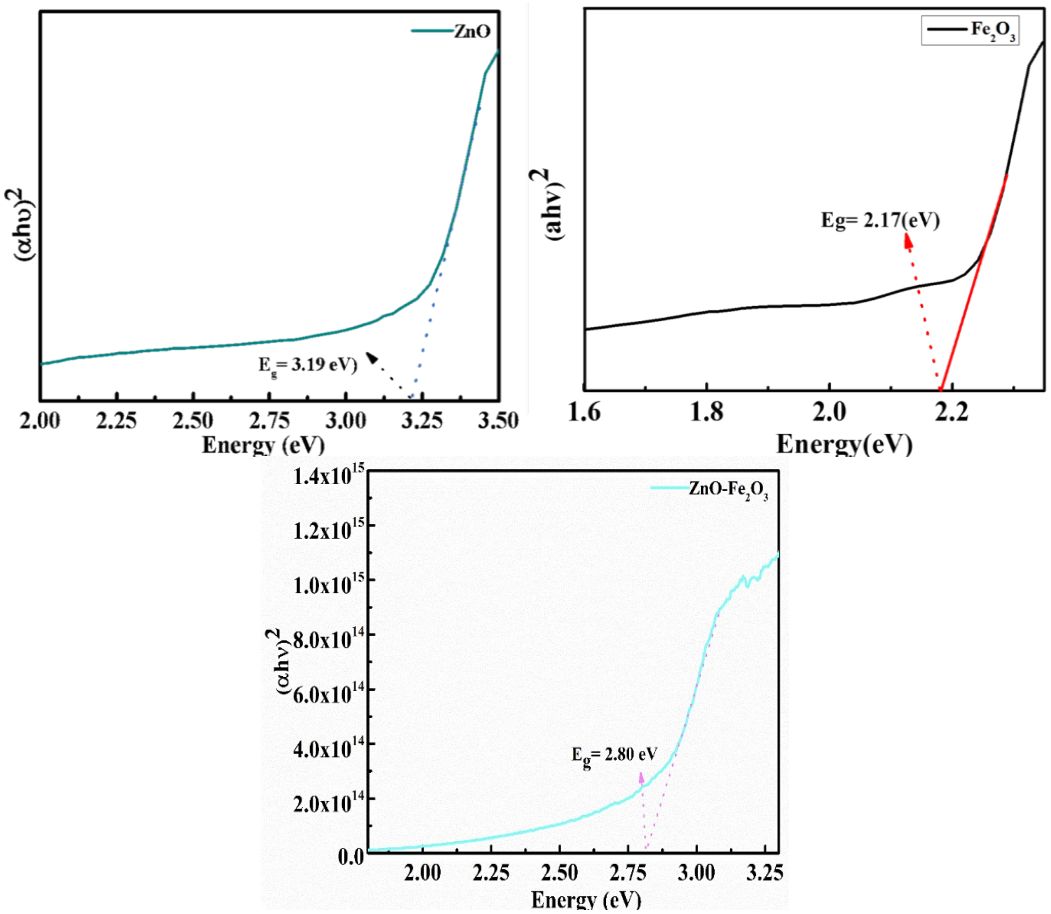


*Fig. 5. Bandgap energy of ZnO, $Fe_2O_3$ and ZnO-$Fe_2O_{3s}$ nano composite.*

The band gap is the lowest energy needed to free a bound electron and allow conduction. The band gap energy calculation relation presented by Tauc is as follows[23].

$$(\alpha hv)^2=B(hv-E_g) \quad (2)$$

where B is a transition probability parameter, energy of photon is hv, and α is an absorption coefficient. Calculated bandgap of $Fe_2O_3$, ZnO, and ZnO-$Fe_2O_3$ nanocomposites are 2.1 eV, 3.1 eV, and 2.8 eV, respectively. For example, ZnO is smaller than a single $Fe_2O_3$ and larger than ZnO-$Fe_2O_3$. $Fe_2O_3$ and ZnO's attraction causes energy bands to emerge between CB and VB, and with very few exceptions, as the number of layers increases, the Eg of materials with layers decreases. (Chaves, 2020). ZnO and $Fe_2O_3$ are two-layered materials. The ZnO-$Fe_2O_3$ nanocomposite has extra layers as a result of the interactions between the layers [24]. Thus, the approach to reduce $E_g$ is to increase the number of layers. The Eg of the nanocomposite can also be affected by the electric field when materials come into contact with one another. To counteract this transfer, electrons travel from one semiconductor to the other that has a greater Fermi energy, creating an electrical field in this process [25]. The relationship between the optical constants of a material and its properties as a function of light is investigated. Using UV–vis spectroscopy, the four most significant optical characteristics that can be determined are the standard index of refraction (n), extinction coefficient (k), the electronegativity (ΔX*), and dielectric constant (d). The refractive index (n), a crucial property of optical materials, explains the bending of light waves as they go through various materials [26]. When assessing a sample's optical properties, one of the most crucial variables is the "n." Refractive index detection is usually employed in the analysis of dyes or materials with limited absorption ranges. It is available as[27]

$$n = 4.08 - 2.3064(\Delta\chi^*) \quad (3)$$

where 4.08 and 2.3064 are constants, and ($\Delta\chi^*$) is optical electronegativity. For $Fe_2O_3$, ZnO and ZnO-$Fe_2O_3$ nanocomposite, the calculated values of "n" are 2.77, 2.10, and 2.33, in that order. Light deflects more in the direction of normal in nanocomposite due to an increase in refractive index. The higher material's refractive index, the slower light travels through it, which leading to a larger shift in direction. Higher "n" was induced by different bonding between ZnO and $Fe_2O_3$, which is because to oxygen vacancies [28]. The following formula yields the extinction coefficients for pure $Fe_2O_3$, ZnO and ZnO-$Fe_2O_3$ [3].

$$k=n/(\Delta X)^{-0.32} \quad (4)$$

It indicates that there is a -0.32 value in the relationship between the refractive index n and the electronegativity differential ΔX*. The calculated values of $Fe_2O_3$, ZnO and ZnO-$Fe_2O_3$, are 2.30, 1.99 and 2.12 in that order. As k increased, surfaces optical scattering and loss increased as well [3]. Understanding optical electronegativity (X*) is essential to understanding chemical bonding. Equation (a) provides the energy band relation, which optical electronegativity may determine [27].

$$\Delta X^*=E_g/3.72 \quad (5)$$

$Fe_2O_3$, ZnO and ZnO-$Fe_2O_3$ have calculated values of 0.56, 0.85 and 0.75, in that order. The existence of optical electronegativity has have an immediate impact on the concept of chemical bonding. Based on its magnitudes, the size of (X*) indicates the type of bonding that exists in the material. A compound is classed as covalently if the magnitude of (X*) is less than that of an ionic compound [29]. The degree of polarity of a medium is determined by its dielectric constant (ε), which is inversely related to the polarisability of solid materials. The meaning of "" in terms of real and imaginary components is provided by the following definition:

$$\varepsilon= \varepsilon_i + \varepsilon_r \quad (6)$$

When the dielectric constant's " $\varepsilon_i$ " and " $\varepsilon_r$ " components are represented as follows.

$$\varepsilon_i = 2nk \tag{7}$$

$$\varepsilon_r = n^2 - k^2 \tag{8}$$

The actual component of light's speed provides information on how much it slows down in a given amount of time. The electric field that absorbs energy due to dipole motion is described by the imaginary part of the equation, which also represents the dielectric properties of a material. One may get the loss factor by dividing εi by εr. Photon energy (hv) has a major effect on the imaginary (εi) and real (εr) components of the dielectric constant. The calculated εr and εi for $Fe_2O_3$, ZnO, and ZnO-$Fe_2O_3$ are displayed in Figure 8 and are, respectively, 0.92, 0.20, and 0.40; and, for ZnO-$Fe_2O_3$, 12.77, 8.39, and 9.92. Here, "decreased real part" means that light travels through a medium at a slower pace. This results in significant light scattering. A gain in absorption of light is referred to as the imaginary component. All samples, however, exhibit εr values that are bigger than εi, suggesting that modifying the concentrations of the various components alters εr and εi values [15, 30].

*Table 1.* An overview of the calculated optical parameters.

| **Samples** | **Eg** | **n** | **K** | **ΔX*** | **εr** | **εi** |
|---|---|---|---|---|---|---|
| FeO | 2.17 | 2.77 | 2.30 | 0.56 | 0.92 | 12.77 |
| ZnO | 3.19 | 2.10 | 1.99 | 0.85 | 0.20 | 8.39 |
| Composite | 2.81 | 2.33 | 2.12 | 0.75 | 0.40 | 9.92 |

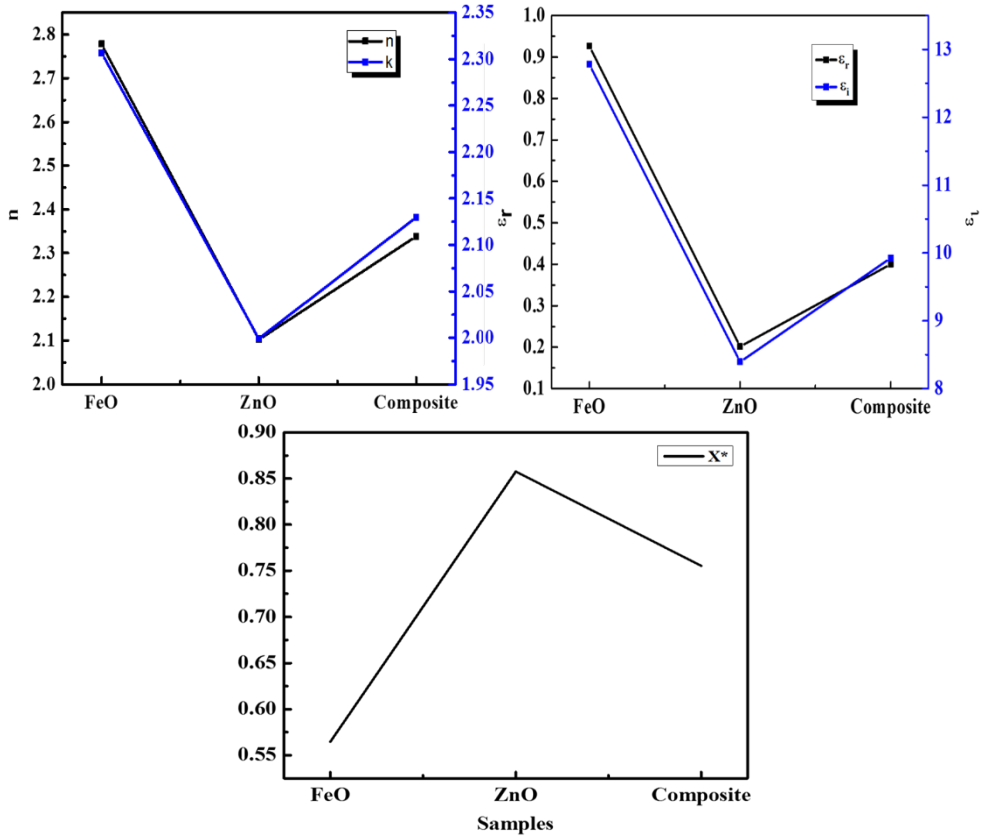


*Fig. 6. Extinction coefficient, Refractive index, and dielectric constant (real & imaginary) and optical electronegativity of ZnO, $Fe_2O_3$ and ZnO-$Fe_2O_3$.*

Figure 6 compares the clearance of dye molecules as a result of irradiation time. The material releases electrons from the valence band (VB) with energy equivalent to its bandgap ($E_g$) when exposed to sunlight. By moving in the direction of the conduction band (CB), these electrons form electron-hole pairs. These electrons combine with oxygen molecules in real time to create radicals that are free of hydroxyl. When it comes to oxidation, one can either mix with water to create radicals devoid of hydroxyls or exploit the natural ability of cavitation to carry out a direct oxidation process.

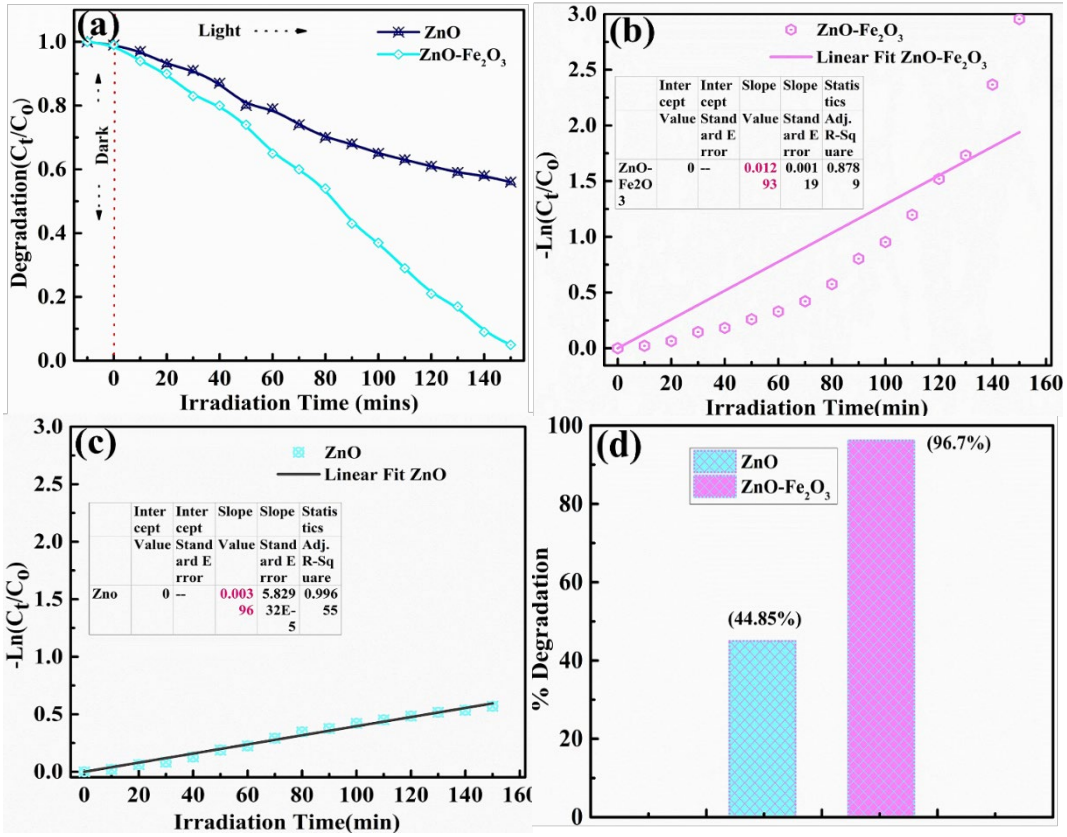


*Fig. 7. Photocatalytic degradation for MB dye (a), Time vs -Ln($C_o/C_t$) (b and c), and percentage degradation (d).*

This mechanism, which is illustrated in Fig. 9 and explained by Liu (2015), highlights the essential ideas behind this photolytic process[31].

$$\text{Catalyst} + \text{light} \rightarrow e^- (\text{CB}) + h^+ (\text{VB}) \tag{9}$$

$$e^- + O_2 \rightarrow O^{\circ -}_2 \tag{10}$$

$$H_2O + h^+ \rightarrow OH^\circ + H^+ \tag{11}$$

$$\text{Organic contaminants (dye Intermediates)} + O^{\circ -}_2 \rightarrow \text{degradation} \tag{12}$$

$$MB + OH^\circ \rightarrow H_2O + CO_2 \tag{13}$$

The MB dye is remarkably well-degraded by the ZnO-$Fe_2O_3$ compound, which also shows remarkable light sensitivity. For MB dye, the degradation efficiency was 81% and 68%, respectively. Strong crystallinity and the composite's distinct morphology which is characterized by agglomerated clusters that improve performance are responsible for its high efficiency. Interestingly, because of its favorable properties such as shorter photo-generated diffusion routes, increased accidental light absorption, effective settling, and a noticeably large surface area—this agglomerated structure is rare in aquatic photocatalytic activity. The interfaces and junctions within the material improve the efficiency of the composite by lowering the recombination rate and guaranteeing the efficient separation of electron-hole pairs during Photocatalysis. The composite's agglomerated cluster morphology, which is clearly visible in the SEM, plays an important role to its exceptional dye degradation efficiency and makes it a viable option for a number of environmental remediation and wastewater treatment applications.

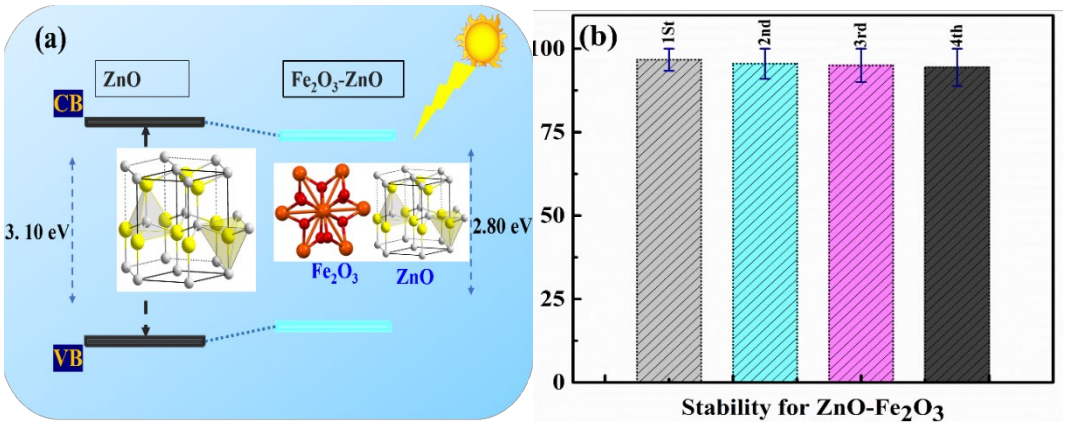


*Fig. 8. Schematic diagram for band structures for ZnO and $Fe_2O_3$-ZnO (a) and degradation stability graph for $Fe_2O_3$-ZnO.*

## 4. Conclusion

In summary, this study investigates the photocatalytic degradation of organic contaminants, focusing on ZnO, $Fe_2O_3$, and the ZnO-$Fe_2O_3$ composite. Prepared through the sol-gel method, these materials are assessed for their potential in environmental remediation. The research underscores the influence of $Fe_2O_3$ doping concentration on the formation of the ZnO-$Fe_2O_3$ nanocomposite. Additionally, X-ray diffraction validates the enhanced crystallinity resulting from interactions between ZnO and $Fe_2O_3$. SEM analysis reveals a highly aggregated structure, promising efficient dye degradation and environmental applications. Photoluminescence (PL) spectra indicate a prominent peak at 377 nm, implying efficient charge separation with potential use in optoelectronic applications. Furthermore, the composite's unique optical properties, including its refractive index, extinction coefficient, and dielectric constants, underscore its versatility. Remarkably, the ZnO-$Fe_2O_3$ nanocomposite, synthesized at 500 °C, exhibits superior photocatalytic activity, particularly in the rapid degradation of Methyl Blue dye under sunlight irradiation.

## Acknowledgements

Researchers Supporting Project number (RSP2024R397), King Saud University, Riyadh, Saudi Arabia

**References**

[1] Zhang, Y., et al., ChemCatChem, 2019. 11(10): p. 2546-2553; https://doi.org/10.1002/cctc.201900278

[2] Bano, S., et al., Journal of Materials Research and Technology, 2022. 19: p. 1982-1992; https://doi.org/10.1016/j.jmrt.2022.05.137

[3] Kanwal, S., et al., Arabian Journal of Chemistry, 2023. 16(5): p. 104685; https://doi.org/10.1016/j.arabjc.2023.104685

[4] Bukhari, M., et al., Diamond and Related Materials, 2023. 132: p. 109631; https://doi.org/10.1016/j.diamond.2022.109631

[5] Arshad, M., et al., Materials Research Express, 2020. 7(1): p. 015407; https://doi.org/10.1088/2053-1591/ab6380

[6] Aldeen, E.S., et al., Chemosphere, 2022. 304: p. 135349; https://doi.org/10.1016/j.chemosphere.2022.135349

[7] Iqbal, M., et al., Materials Research Express, 2020. 7(1): p. 015070; https://doi.org/10.1088/2053-1591/ab692e

[8] Khana, M., et al., Chalcogenide Letters, 2022. 19(2): p. 75-82; https://doi.org/10.15251/CL.2022.192.75

[9] Bashir, M., et al., Arabian Journal of Chemistry, 2022. 15(11): p. 104194; https://doi.org/10.1016/j.arabjc.2022.104194

[10] Khan, M., et al., Ceramics International, 2023.

[11] Mishra, M., D.-M. Chun, Applied Catalysis A: General, 2015. 498: p. 126-141; https://doi.org/10.1016/j.apcata.2015.03.023

[12] Noreen, S., et al., Ceramics International, 2022. 48(9): p. 12170-12183; https://doi.org/10.1016/j.ceramint.2022.01.078

[13]. Mustafa, G., et al., Physica B: Condensed Matter, 2023. 663: p. 415006; https://doi.org/10.1016/j.physb.2023.415006

[14] Din, A., et al., Journal of Molecular Liquids, 2017. 237: p. 266-271; https://doi.org/10.1016/j.molliq.2017.04.060

[15] Mujtaba, A., et al., Journal of Materials Research and Technology, 2023. 23: p. 4538-4550; https://doi.org/10.1016/j.jmrt.2023.02.038

[16] Mohamed, H.H., et al., Journal of Photochemistry and Photobiology A: Chemistry, 2019. 382: p. 111951; https://doi.org/10.1016/j.jphotochem.2019.111951

[17]. Chaim, R., et al., Journal of Materials Science, 2018. 53: p. 3087-3105; https://doi.org/10.1007/s10853-017-1761-7

[18] Widiarti, N., J. Sae, S. Wahyuni. IOP Conference Series: Materials Science and Engineering. 2017. IOP Publishing; https://doi.org/10.1088/1757-899X/172/1/012036

[19] Bibi, I., et al., Journal of Materials Research and Technology, 2019. 8(6): p. 6115-6124; https://doi.org/10.1016/j.jmrt.2019.10.006

[20] Khan, M., et al., Results in physics, 2017. 7: p. 651-655; https://doi.org/10.1016/j.rinp.2016.12.029

[21] Galdámez-Martinez, A., et al., Nanomaterials, 2020. 10(5): p. 857; https://doi.org/10.3390/nano10050857

[22] Singh, S., G. Hitkari, and G. Pandey, Inorganic and Nano-Metal Chemistry, 2018. 48(10): p. 477-485; https://doi.org/10.1080/24701556.2019.1571511

[23] Khan, M., et al., Results in physics, 2017. 7: p. 1437-1439 https://doi.org/10.1016/j.rinp.2017.03.023

[24] Rahmah, M.I., R.S. Sabry, W.J. Aziz, International Journal of Minerals, Metallurgy and Materials, 2021. 28(6): p. 1072-1079; https://doi.org/10.1007/s12613-020-2096-y

[25] Chaves, A., et al, Materials and Applications, 2020. 4(1): p. 29; https://doi.org/10.1038/s41699-020-00162-4

[26] Khan, M.I., et al., Coatings, 2022. 12(3): p. 386; https://doi.org/10.3390/coatings12030386

[27] Bahadur, A., M. Mishra, Acta Physica Polonica A, 2013. 123(4): p. 737-740; https://doi.org/10.12693/APhysPolA.123.737

[28] Qin, Q., et al., Journal of Hazardous Materials, 2021. 419: p. 126447; https://doi.org/10.1016/j.jhazmat.2021.126447

[29] Wemple, S., M. DiDomenico Jr, Physical Review B, 1971. 3(4): p. 1338; https://doi.org/10.1103/PhysRevB.3.1338

[30] Zulqarnain, M., et al., Journal of Materials Science, 2023: p. 1-23; https://doi.org/10.1007/s10853-023-08906-5

[31] Noreen, S., et al., Environmental Technology & Innovation, 2021. 22: p. 101430; https://doi.org/10.1016/j.eti.2021.101430